

# Spatiotemporal Analyses of Earthquake Productivity and Size Distribution: Observations and Simulations

by A. Ziv\*, A. M. Rubin, and D. Kilb†

**Abstract** We use relocated catalogs of microearthquakes to investigate earthquake interaction along sections of the Sargent, Calaveras, and San Andreas faults in California. We examine the stress dependence of seismicity rate change along the three fault segments and find that the seismicity rate following a mainshock decays approximately as  $1/\text{time}$ , the duration of the aftershock activity seems to be independent of distance from the mainshock, and the seismicity rate at lag times of up to about 100 sec is nearly constant. In the San Andreas and the Calaveras catalogs, where the return of the seismicity rate to the background level is well resolved, we find that the return to the background in the distance range of 1–2 rupture radii from a previous earthquake is preceded by a period during which the seismicity rate falls about 30% below the background rate. We also examine the effect of a stress step on earthquake size distribution along these faults and find that the exponent of the power-law distribution of earthquake magnitudes within  $10^4$  sec of a previous earthquake is significantly lower than that of the long term. While the  $1/\text{time}$  decay of seismicity rate, the independence of aftershock duration from distance from the mainshock, and the constant seismicity rate at short lag times are predicted by Dieterich's (1994) model, the decrease of seismicity rate below the background level and the changes in earthquake size distribution are not.

For comparison with our observations, we simulate earthquake activity on an inherently discrete fault model that is governed by an approximate constitutive friction law similar to the one used by Dieterich (1994). We find that the observed response of earthquake productivity and size distribution to a stress step are produced by these simulations. The effect of the mainshock is not only to raise the local seismicity rate, but also to systematically modify the earthquake size distribution. This is because fault patches that are near failure at the time of the stress step are strengthened, whereas fault patches that at the same time were far from failure are weakened. As a result, similar to what is observed for the Calaveras and the San Andreas segments, late during the aftershock sequence the seismicity rate may decrease below the background rate. We suggest that the time-dependent modification of the earthquake size distribution by a stress step can explain observations of lower  $b$ -values immediately following a stress step.

## Introduction

The primary use of microearthquakes in the past has been to illuminate fault structures (e.g., Seeber and Armbruster, 1995; Carena and Suppe, 2002) and to investigate aftershock sequences associated with large earthquakes (e.g., Gross and Kisslinger, 1997; Toda *et al.*, 1998). Several re-

cent efforts to reduce errors in relative location between earthquakes have yielded sharper fault images (Got *et al.*, 1994; Schaff *et al.*, 1998; Shearer, 1998; Rubin *et al.*, 1999; Shaw and Shearer, 1999; Waldhauser *et al.*, 1999; Kilb and Rubin, 2002). In the process of improving relative earthquake locations, location errors between nearby events have been reduced from hundreds of meters to meters or at most a few tens of meters. This is much smaller than the estimated rupture dimensions of many tens to hundreds of meters. Thus, apart from providing sharper fault images, relocated

\*Present address: Laboratoire de Géologie, Ecole Normale Supérieure, 24 Rue Lhomond, 75231 Paris France.

†Present address: IGPP, University of California, San Diego, La Jolla, California, 92093.

catalogs may be used to examine interaction between microearthquakes.

Dieterich (1994) modeled the response to a stress step of a population of faults governed by rate- and state-dependent friction. This model has gained considerable popularity, as it predicts the decay with time of seismicity rate according to the modified Omori's law. In addition, according to this model both the magnitude and the duration of aftershock activity are related to fault constitutive parameters. Because these quantities are observable, the model predictions are testable and may be used to interpret natural aftershock sequences. Dieterich's model, however, relies on several simplifying assumptions. In addition to assuming that aftershocks nucleate over areas of the fault that at the time of the mainshock are already accelerating toward failure, Dieterich disregarded the effect of interactions among aftershocks and assumed that the earthquake size distribution is time independent. In a previous study, Ziv and Rubin (2003) presented an inherently discrete fault model, with a fault surface governed by an approximate constitutive friction law similar to the one used by Dieterich. The main purpose of that study was to examine consequences of relaxing the assumptions underlying Dieterich's model. In this study, the same fault model is used to examine whether observed spatiotemporal clustering of earthquakes is consistent with that of a fault that is governed by rate- and state-dependent friction.

We use relocated catalogs of seismicity from California to examine the effects of stress changes on seismicity rate and size distribution along sections of the Calaveras, Sargent, and San Andreas faults (Fig. 1). We find that the effect of a stress change is not only to modify the seismicity rate, but also to perturb the earthquake size distribution in a manner that is consistent with models of a fault governed by rate- and state-dependent friction.

## Observed Earthquake Interactions

### The Composite Catalogs

Several thousand microearthquakes in northern California have been relocated using a waveform cross-correlation technique (Got *et al.*, 1994; Rubin *et al.*, 1999; Rubin, 2002). These catalogs span a period of about 15 years (March 1984–January 1998). From this data set, we have extracted earthquakes from a section of the San Andreas fault, the Calaveras fault, and the Sargent fault (Fig. 1). Since here we wish to examine interaction between microearthquakes, we seek a data set that is not (or is only slightly) affected by large earthquakes. The two major earthquakes that occurred in the study area during the time period covered by the catalogs are the  $M$  6 1984 Morgan Hill and the  $M$  7 1989 Loma Prieta. Plots of earthquake rate in the Northern California Seismic Network Catalog as a function of time following these earthquakes indicate that the Loma Prieta earthquake only slightly affected the seismicity in the study areas, while

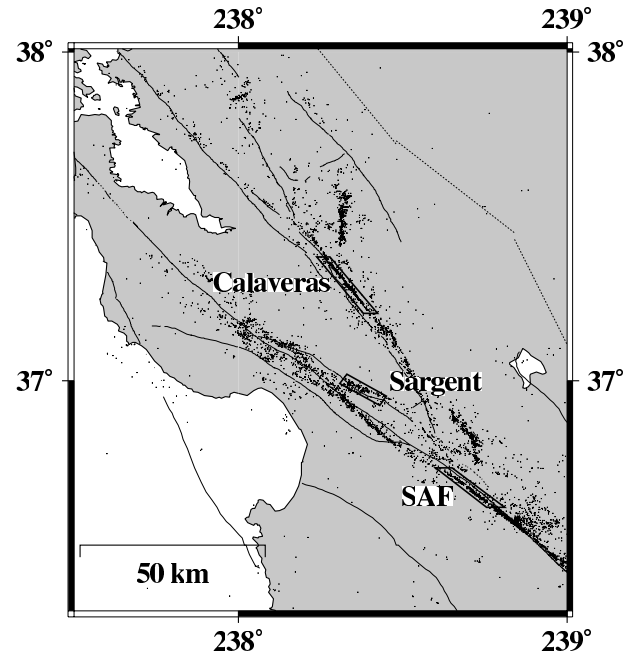


Figure 1. Map of seismicity, showing every tenth earthquake recorded by the Northern California Seismic Network between January 1969 and January 1998. Solid lines indicate active faults (Jennings, 1992). Boxes show the three regions within which earthquakes were relocated and analyzed in this study. SAF, San Andreas fault.

the Morgan Hill significantly increased the seismicity rate along the Calaveras fault. In an attempt to remove the effect of the Morgan Hill earthquake, we have disregarded about 1700 events that occurred within this 1000-day window.

Because the seismicity along these fault segments is coplanar and the focal mechanisms are almost identical, the effect of every earthquake on all later nonoverlapping earthquakes is to raise the static shear stress, but (except for possible small-scale geometric heterogeneities that we neglect) not the normal stress. The stress that a given rupture induces at the hypocenter of a later rupture is a function of the stress drop of the first event and the distance between the two hypocenters normalized by the radius of the first rupture. We compute rupture dimensions using the moment–magnitude relationship of Abercrombie (1996) and the scaling of slip with length on a circular crack of Eshelby (1957), assuming stress drops of 10 MPa. Throughout this article, we refer to the ratio between the interevent distance and the radius of the early event as normalized distance. For normalized distance greater than about 3, the stress change scales as the seismic moment divided by the distance cubed and is thus insensitive to the assumed stress drop.

We take a rather unusual approach of treating each relocated earthquake as if it were a mainshock. Consequences of this approach are examined in a later section using synthetic catalogs. Lag times (i.e., the difference between origin times) and normalized distances between every event and all

later events are calculated. Since, as we will show later, aftershock duration in the studied areas may last up to 100 days, and since we wish to resolve the return of the seismicity rate toward the background level, it was necessary to consider lag times that are a few times larger than the aftershock relaxation time. Therefore, mainshock–aftershock pairs with lag times of up to 500 days are stacked to give a composite catalog. Earthquakes that occurred during the last 500 days of the original catalog were not considered as mainshocks. The exclusion of these mainshocks was intended to ensure that the analysis is not sensitive to the length of the original catalog or affected by its end. Choosing a time window much larger than 500 days would have worsened the resolution of our result, as a greater number of earthquakes would have been eliminated from the foreshocks list. The new catalog is binned according to normalized distance.

A type of mainshock–aftershock pair that is accounted for here, but not in other studies of aftershock sequences (e.g., Gross and Kisslinger, 1997), is an aftershock of an aftershock. For example, consider two nearby small earthquakes that followed a large earthquake (Fig. 2a). The stress induced on the late small earthquake by the early small earthquake may be larger than that induced by the large earthquake. In our scheme, we count the later of the small earthquakes once as an aftershock of the large earthquake and once again as an aftershock of the early small earthquake. A disadvantage of this scheme is that it does not distinguish “real” from “apparent” mainshock–aftershock pairs. For example, consider two distant small earthquakes that followed a large earthquake (Fig. 2b). In this example, the second aftershock is counted once as an aftershock of the mainshock and once as an aftershock of the first aftershock. The first may be regarded a real mainshock–aftershock pair, whereas the latter is an example of an apparent mainshock–aftershock pair. Although it might be possible to come up with an alternative definition of a mainshock–aftershock pair, such that most of the apparent pairs would be excluded from the composite catalog, different schemes suffer from other disadvantages, and we have not yet devised an ideal alternative. All the conclusions of this study are drawn based on a comparison between time-space analyses performed on natural and synthetic composite catalogs that are stacked using the same technique. Since any bias that exists in the analyses of the natural catalogs exists also in the analyses of the synthetic catalogs, the disadvantages of the stacking procedure are not a major problem.

#### Spatiotemporal Analysis of Earthquake Productivity

We plot seismicity rate change as a function of lag time, binned according to ranges of normalized distance of 0.8–2, 2–4, 4–8, and 8–16, for sections of the Sargent fault, the San Andreas fault, and the Calaveras fault (Fig. 3). Seismicity rates were calculated for moving overlapping time windows. The first window of every plot contains  $N_0$  data points, and

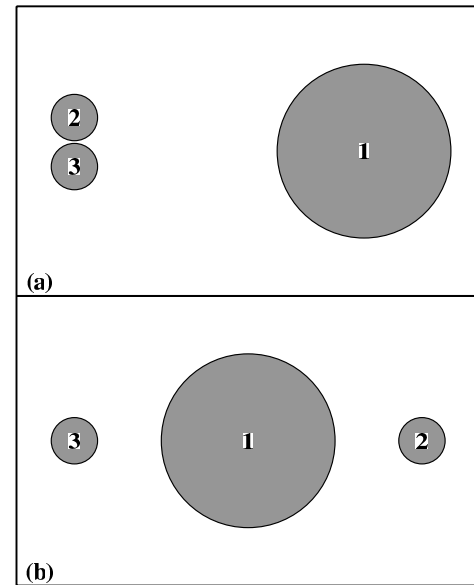


Figure 2. Examples of mainshock–aftershock pairs: (a) event 3 is an aftershock of event 2, which itself is an aftershock of event 1, and (b) event 3 is an aftershock of event 1 and an apparent aftershock of event 2. The numbers signify the order in which the earthquakes rupture.

the window slides by one data point and increases its capacity by  $\Delta N$  data points each time, with a maximum allowed number of data points of  $N_{\max}$ . The choice of  $N_0$ ,  $\Delta N$ , and  $N_{\max}$  is indicated in each frame. Seismicity rates were normalized by background rates, which for each distance range were computed based on the average seismicity rate during the time interval 300–500 days.

This scheme, of sliding the time window by one data point each time, results in significant overlapping between adjacent windows. In Figure 4 we show, for the San Andreas fault, a similar calculation with no overlapping between bins. Note that while overlapping between adjacent bins creates a strong smoothing, the main features in Figures 3b remain unchanged in the absence of such overlapping. We performed similar calculations for the Sargent and the Calaveras faults (not shown) and reached the same conclusion.

Aftershock response along the three fault segments differs in that the seismicity rate change is more sensitive to distance from the mainshock on the Sargent fault than on the San Andreas and Calaveras faults. In addition, the seismicity response is stronger and lasts longer along the Sargent fault than along the Calaveras. The San Andreas fault exhibits intermediate characteristics.

Seismicity responses along the three fault segments share several important characteristics. In all cases, the seismicity rate decays approximately as  $1/\text{time}$ . In addition, the duration of the aftershock activity seems to be independent of distance from the mainshock. For the Calaveras fault, seismicity curves at lag times of up to about 100 sec are

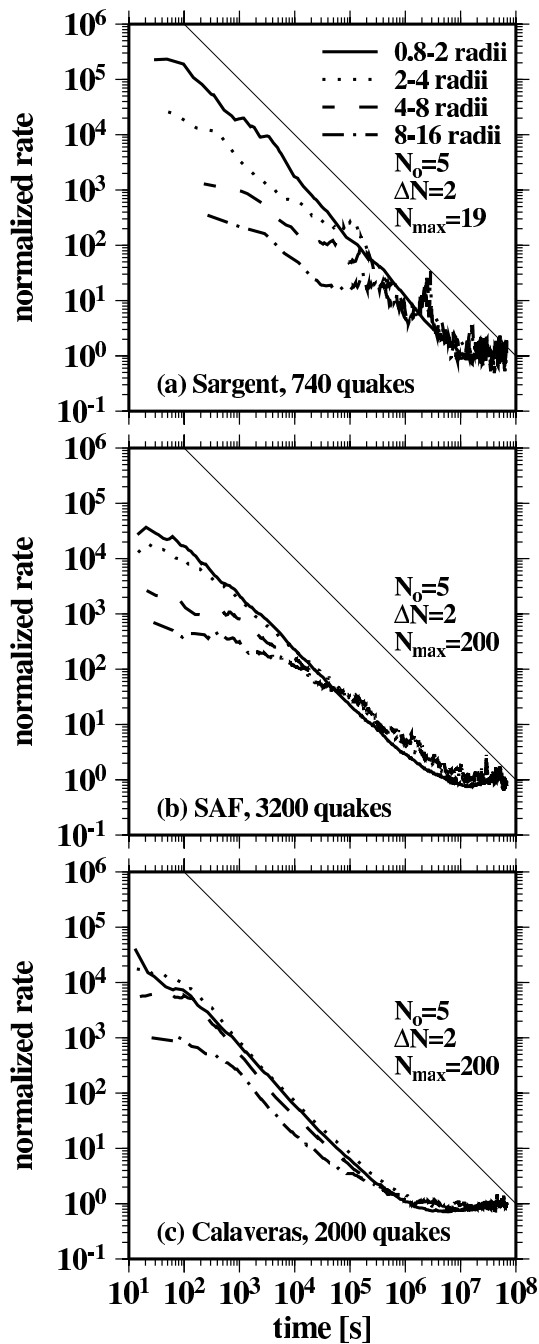


Figure 3. Normalized seismicity rates as a function of time, binned according to four distance ranges, observed along segments of (a) the Sargent fault, (b) the San Andreas fault, and (c) the Calaveras fault (Fig. 1). Seismicity rates were calculated for moving overlapping time windows. The first window of every plot contains  $N_0$  data points; the window slides by one data point and increases its capacity by  $\Delta N$  data points each time, with a maximum allowed number of data points of  $N_{\max}$ . Seismicity rates are normalized by the rate computed for the time interval between 300 and 500 days. For reference, the thin line in each diagram indicates a slope of  $1/t$ .

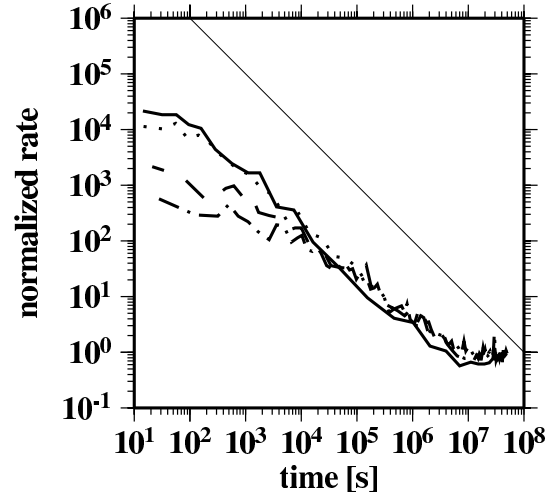


Figure 4. Normalized seismicity rates as a function of time, binned according to four distance ranges, observed along a segment of the San Andreas fault. Seismicity rates were calculated for moving nonoverlapping time windows and with  $N_0$ ,  $\Delta N$ , and  $N_{\max}$  as in Figure 3b.

nearly flat. Also for the Sargent and the San Andreas faults, some flattening is seen.

In principle, since the flattening of the seismicity curves occurs at very short lag times, during which the ground shaking produced by a previous earthquake may limit the detection of aftershocks, the observed flattening should be interpreted with caution. In addition, since for a given curve the number of data points used to determine the aftershock rate increases with time since the mainshock, the flat portion of the seismicity curves relies on a particularly small number of data. Thus, trying to test the possible influence of missed aftershocks on this result is very difficult. Nevertheless, a number of lines of evidence suggest that the flattening of the seismicity curves may not just be an artifact of catalog incompleteness. First, nearby earthquake pairs with lag times of less than 10 sec are recorded by the network, even in cases where the second event is the smaller of the two. In addition, inspection of seismograms shows that the noise level more than 30 sec after a magnitude 2 event is quite small at most stations. Finally, the best evidence that catalog incompleteness is not a major problem may be the decay according to  $1/t$  in the nearest region (solid curve) for lag times greater than 10 sec in Figure 3c, coupled with the flattening between 10 and 100 sec in successively larger distance ranges.

Dieterich (1994) modeled the response to a single stress step of a population of faults governed by rate- and state-dependent friction. The  $1/\text{time}$  decay of seismicity rate, the independence of aftershock duration from distance from the mainshock, and the flattening at short lag times (with a maximum rate that increases with the size of the stress step) are predicted by this model.

Note that for the San Andreas and the Calaveras catalogs, for which (owing to the catalog size) the statistics are

most reliable, the return of seismicity to the background level in the nearest distance range appears to be preceded by a period during which the seismicity rate falls about 30% below the background rate (Fig. 5). This feature is not predicted by Dieterich's analytical model but is reproduced by some of the numerical simulations discussed later.

#### Spatiotemporal Analysis of Earthquake Size Distribution

The parameter used to measure size distribution of an earthquake catalog is the  $b$ -value, where  $b$  refers to the exponent of the power-law distribution of earthquake magnitudes. A low  $b$ -value indicates a high ratio of large to small earthquakes and therefore a higher risk for a given earthquake rate. Because the  $b$ -value need not be constant over the magnitude range of interest, we plot the raw data (number of earthquakes as a function of magnitude) rather than fitting these data with a straight line when such a fit may not be warranted.

Frequency-size distributions of relocated earthquakes in areas confined to 0.8–4 radii from a previous relocated earthquake are compared for two consecutive time windows (Fig. 6). Due to the possibility of missed small aftershocks hidden in the coda of previous mainshocks, the average magnitude of recorded aftershocks that occurred shortly following a mainshock might be higher than the actual average. To ensure that the results of our analysis are not sensitive to this type of bias, we apply several restrictions. In Figure 6a–c, mainshock–aftershock pairs with lag times of less than 30 sec were excluded from the analysis. We find, for the three fault segments, higher ratios of large to small earthquakes (i.e., a lower  $b$ -value) early in the aftershock sequence as compared to later in the aftershock sequence. In addition to excluding pairs with lag times of less than 30 sec, we excluded pairs if the mainshock magnitude was greater than 2 (Fig. 6d–f) or if the mainshock magnitude was greater than the aftershock magnitude by more than 0.5 (Fig. 6g–i). In all cases, the ratio of large to small earthquakes decreases with elapsed time since the mainshock.

Clearly the analysis of an individual fault relies on a rather small amount of data (especially for the Sargent fault). This may cast doubt on the statistical significance of this result. We would like to test the null hypothesis that the differences in the size distributions between the two consecutive time windows may arise by chance. For that purpose, we computed frequency-size distributions for synthetic catalogs produced by shuffling the magnitudes in the original catalogs (but with rupture dimensions that are calculated based on the “true” magnitudes). In Figure 7, observed size distributions for time intervals as in Figure 6a–c are compared to 50 synthetic frequency-size distributions. To test the null hypothesis, we calculated the joint probability for the size distribution curves of synthetic catalogs to exceed the solid curves in Figure 6a–c at early time intervals and for the size distribution curves of synthetic catalogs to fall below the dotted curves in Figure 6a–c at later time

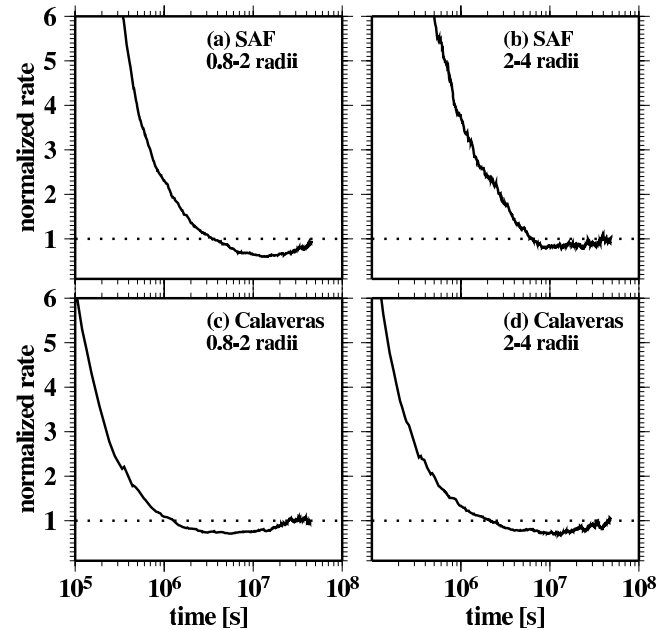


Figure 5. Enlarged view of the decay of seismicity rate toward the background: (a) the San Andreas fault in the distance range of 0.8–2 rupture radii, (b) the San Andreas fault in the distance range of 2–4 rupture radii, (c) the Calaveras fault in the distance range of 0.8–2 rupture radii, and (d) the Calaveras fault in the distance range of 2–4 rupture radii. Note that the return of seismicity to the background level is preceded by a period during which the seismicity rate falls below the background rate, particularly in the distance range of 0.8–2 radii.

intervals. For each of the three catalogs, we find that the null hypothesis can be rejected with a confidence level greater than 99%.

Correlations between stress changes and  $b$ -value changes are strongly implied in several studies of aftershock sequences of large earthquakes. For example, Hosono and Yoshida (2002) compared decay rates of aftershocks of different magnitude and observed faster decay rates for big aftershocks than for small ones. Since their analysis included aftershocks that occurred in regions that were unloaded by the mainshock, comparison between their result and ours is not straightforward. Nevertheless, since most aftershocks did occur in regions that were brought closer to failure by the mainshock, their conclusion that large events decay faster than small events and our conclusion that the  $b$ -value early during the aftershock sequence is smaller than the  $b$ -value later during the sequence might be different descriptions of the same phenomenon. Weimer and Katsumata (1999) compared the spatial distribution of coseismic slip during four major earthquakes with the spatial distribution of the  $b$ -values of their aftershocks. They found in all cases higher  $b$ -values along portions of the fault that experienced large slip and smaller  $b$ -values along portions of the fault that experienced little or no slip. Because, in general, one

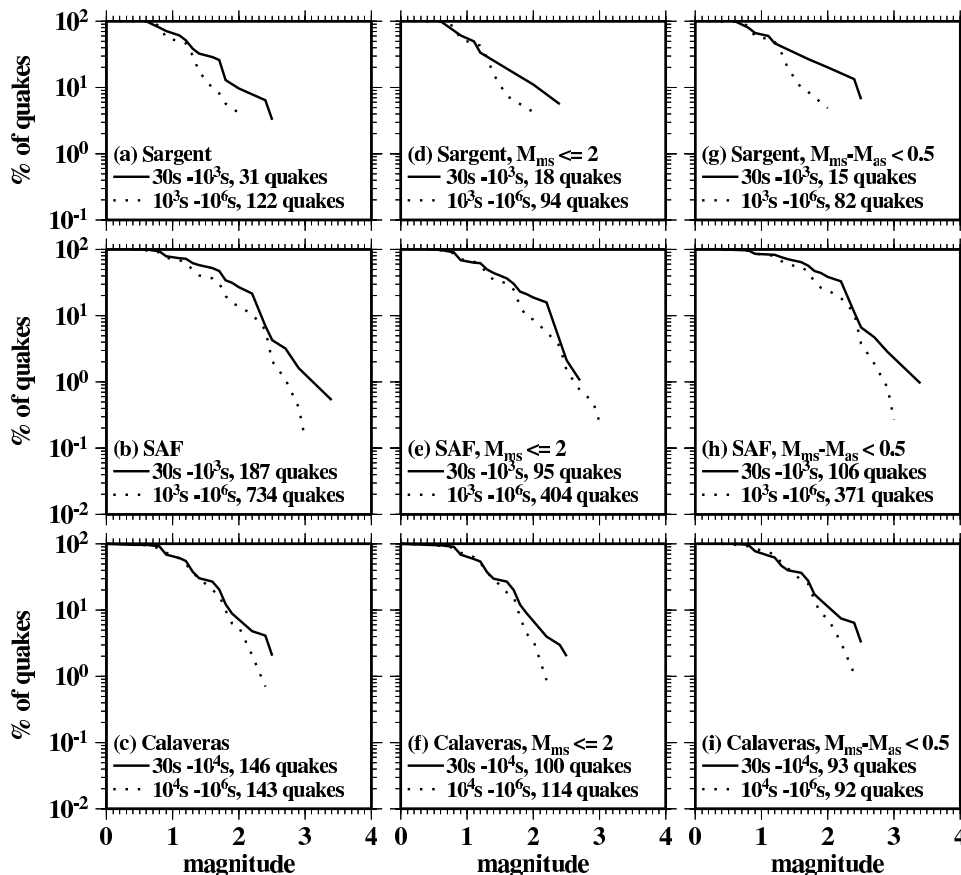


Figure 6. Observed frequency-size distributions of relocated earthquakes in areas confined to 0.8–4 radii from previous relocated earthquakes are plotted for two consecutive time intervals. (a–c) Mainshock–aftershock pairs with lag times of less than 30 sec are excluded. (d–f) Mainshock–aftershock pairs with lag times of less than 30 sec or with a mainshock magnitude greater than 2 are excluded. (g–i) Mainshock–aftershock pairs with lag times of less than 30 sec or with a mainshock magnitude that is greater than the aftershock magnitude by more than 0.5 are excluded. Note that in all cases, the slopes of the frequency-size distributions increase with time since the mainshock.  $M_{ms}$  is the mainshock magnitude, and  $M_{as}$  is aftershock magnitude.

expects the stress to decrease on fault patches undergoing large slip but to increase on fault patches undergoing little slip relative to their surroundings, their observation also suggests that the effect of a stress change is to modify the  $b$ -value in a manner that is consistent with our observation.

In summary, we find that the seismicity rate decays asymptotically as  $1/\text{time}$  and that the duration of the aftershock activity is independent of distance from the mainshock. In addition, seismicity rate curves flatten at lag times smaller than 100 sec. We note that these observations are predicted by Dieterich's (1994) model of aftershock production. For the San Andreas and the Calaveras catalogs, the return of seismicity to the background level in the nearest distance range appears to be preceded by a period during which the seismicity rate falls about 30% below the background rate. Finally, we find that the  $b$ -value during the  $10^3$ - to  $10^4$ -sec interval following a previous earthquake is significantly lower than that of the long term. In the next section we

present the results of a numerical study that shows that these results are expected from faults that are governed by rate- and state-dependent friction.

### Simulated Earthquake Interactions

As mentioned earlier, the observed seismicity response to a stress step is similar to that predicted by Dieterich's (1994) aftershock model. Dieterich's model, however, relies on several simplifying assumptions. In addition to assuming that aftershocks nucleate on fault patches that prior to the mainshock were close to instability, Dieterich disregarded the effect of multiple interactions among aftershocks and assumed that aftershock size distribution is time independent. The results of earthquake simulations that aimed to explore the consequences of relaxing these assumptions were presented in Ziv and Rubin (2003). A brief description of that simulation follows.

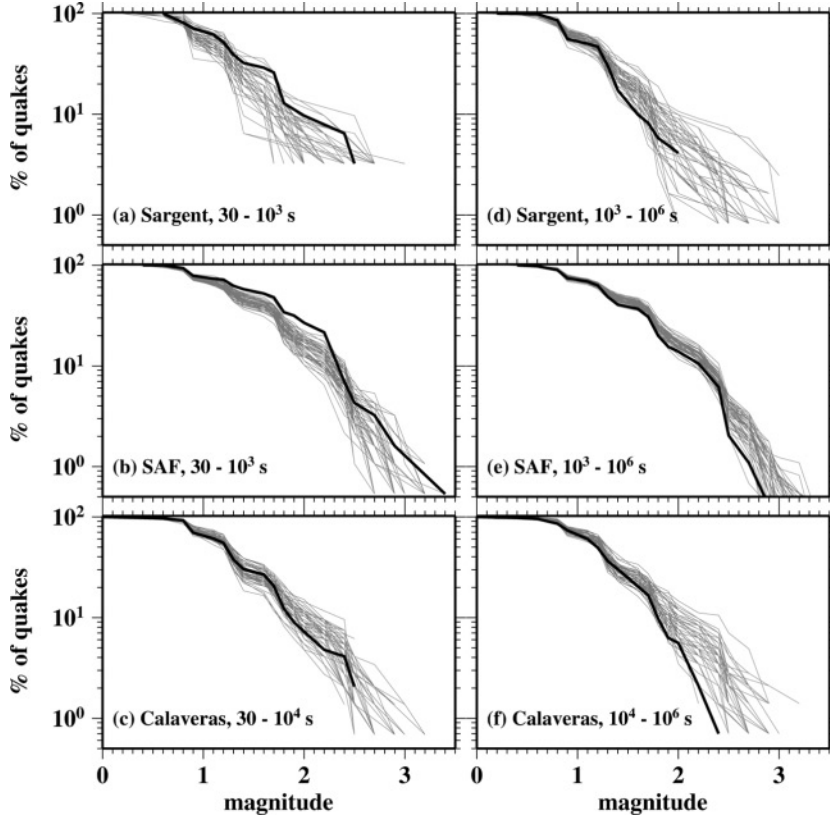


Figure 7. Observed frequency-size distributions in areas confined to 0.8–4 radii from a previous relocated earthquake (solid lines) compared to frequency-size distributions of 50 synthetic catalogs produced by shuffling the magnitudes of the original catalogs (thin gray lines): (a) on the Sargent fault for events with lag times between 30 and  $10^3$  sec, (b) on the San Andreas fault for events with lag times between 30 and  $10^3$  sec, (c) on the Calaveras fault for events with lag times between 30 and  $10^4$  sec, (d) on the Sargent fault for events with lag times between  $10^3$  and  $10^6$  sec, (e) on the San Andreas fault for events with lag times between  $10^3$  and  $10^6$  sec, and (f) on the Calaveras fault for events with lag times between  $10^4$  and  $10^6$  sec.

### The Simulation

Because the observed richness of slip complexity cannot be reproduced by continuous fault models (not even fully dynamic), we turn to an inherently discrete model, capable of producing a power-law size distribution of model earthquakes over a wide range of sizes and spatiotemporal clustering similar to what is observed for natural faults. The fault is modeled as a periodic shear crack with uniform properties embedded in an elastic medium. The fault is stressed at a constant rate  $\dot{\tau}_{\text{tect}}$  in a manner intended to mimic a constant tectonic displacement rate applied at distance  $W$  on either side of the fault. The fault surface is governed by an empirically derived rate- and state-dependent friction law, in which the effects of sliding rate  $\dot{\delta}$  and fault state  $\theta$  on shear stress  $\tau$  are as follows (Dieterich, 1979; Ruina, 1983):

$$\tau = \sigma[\mu_0 + A \ln(\dot{\delta}/\dot{\delta}_*) + B \ln(\theta/\theta_*)]. \quad (1)$$

Here  $A$  and  $B$  are dimensionless constitutive parameters,  $\sigma$  is the effective normal stress,  $\mu_0$  is the nominal coefficient of friction, and  $\dot{\delta}_*$  and  $\theta_*$  are reference velocity and state, respectively. Various physical properties of the fault surface, such as porosity, contact area, and contact age, evolve with slip and elapsed time. The evolution of these properties is embodied in the state parameter. The following evolution law is adopted in this study (Ruina, 1980):

$$\frac{d\theta}{dt} = 1 - \frac{\theta\dot{\delta}}{D_c}, \quad (2)$$

where  $D_c$  is a characteristic sliding distance. Following Dieterich (1995), the evolution of a fault element throughout the seismic cycle is separated into three distinct phases (Fig. 8). For each phase, approximations are made that simplify the governing equations.

Throughout most of the seismic cycle the fault is nearly locked, stress is less than the steady state frictional strength for the given fault state, fault state increases almost linearly with time, and the fault strengthens. This part of the seismic cycle is approximated as a locked fault. For a locked fault, the second term in equation (2) vanishes, and the evolution law becomes  $\theta = \theta_0 + t$ , where  $t$  is time and  $\theta_0$  is the state at  $t = 0$ .

Later in the cycle, sliding velocity increases, the stress exceeds the steady state strength, the state decreases, and the fault weakens rapidly. This part of the seismic cycle is approximated as Dieterich's self-accelerated phase. Because sliding velocity at this stage is high, the first term in equation (2) may be neglected and the evolution law becomes  $\theta = \theta_0 \exp(-\delta/D_c)$ , where  $\delta$  is slip. Using this approximation, Dieterich obtained several analytical expressions describing the evolution of sliding on a self-accelerating crack (Dieterich, 1992) and the change in seismicity rate resulting from

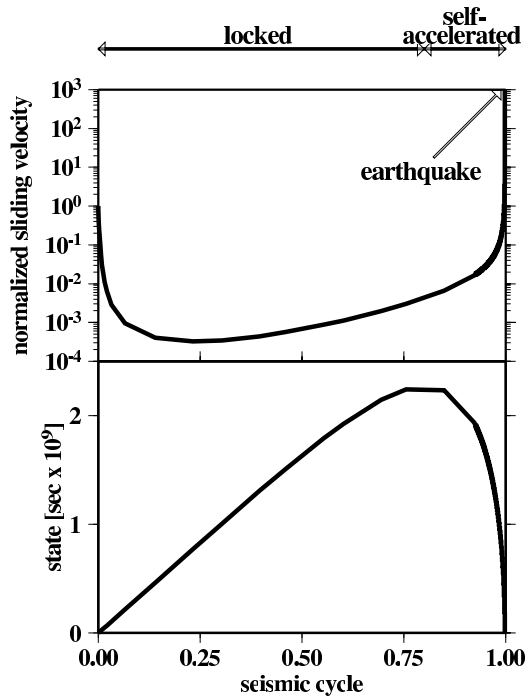


Figure 8. An example of the evolution of sliding velocity normalized by loading point velocity (top) and fault state (bottom) throughout a single seismic cycle, obtained via exact solution of the spring-slider system as in Gombert *et al.* (1997). At the start of the cycle, the slider decelerates over a timescale that is indicative of the healing rate. From the start to 75% of the cycle, the state increases almost linearly with time, and the sliding velocity is well below that of the loading point. This portion of the cycle is approximated as locked. During the final 25% of the cycle, the state decreases rapidly and the slider accelerates. This portion of the cycle is approximated as self-accelerated. Finally, sliding velocity reaches the seismic sliding velocity. This occurrence represents the earthquake.

a stress step imposed on a collection of such cracks (Dieterich, 1994).

An earthquake occurs when the sliding velocity reaches the seismic sliding velocity. The stress drop during the earthquake is assumed instantaneous. The stress transfer is governed by static elastic interactions between square boundary elements, each with a uniform displacement discontinuity. In order to eliminate the azimuthal dependency of stress transfer, Poisson's ratio is set to zero. In addition to elastic interaction between elements, elements are stressed according to the difference between the local slip and that of the boundary at distance  $W$ . A rupture may grow beyond the size of a single cell if the stress increase on cells in the immediate vicinity of the rupture is large enough to bring the initial sliding velocity instantaneously to the seismic sliding velocity. The subset of cells that makes up the rupture set is determined by iteration. Motivated by the results of elastodynamic models (Madariaga, 1976; Rice and Tse, 1986; Co-

chard and Madariaga, 1996) that show the final slip at the end of the rupture to be larger than that expected from the difference between the rupture strength and the steady state friction at seismic slip speeds, a dynamic-like stress overshoot is added by randomly specifying an overshoot value within the predetermined range of 5%–30%.

In summary, the evolution of a seismic cell throughout a single seismic cycle follows three steps. At the start of the cycle the cell is locked. A locked cell becomes self-accelerating when the stress exceeds the steady state friction at the current state. A self-accelerating cell becomes an earthquake cell when the sliding velocity reaches the predefined seismic sliding velocity. Finally, a seismic cell becomes locked when the stress is less than the steady state friction for sliding at seismic speed.

#### What Controls the Simulated Catalogs?

The set of governing equations in nondimensional form is a function of three main parameters:  $B/A$ ,  $A\sigma\dot{\delta}_{\text{seis}}/\dot{\tau}_{\text{tect}}D_c$ , and  $W/L$ , where  $\dot{\delta}_{\text{seis}}$  is the sliding velocity during an earthquake and  $L$  is the cell half-length. While  $B/A$  and  $A\sigma\dot{\delta}_{\text{seis}}/\dot{\tau}_{\text{tect}}D_c$  contain information regarding the constitutive parameters,  $W/L$  is a geometrical parameter that measures the coarseness of the computational grid with respect to  $W$ . An additional controlling parameter that we added to the simulation is the range of stress overshoot. Ziv and Rubin (2003) explored the effect of the controlling parameters on properties of the simulated seismicity, such as average stress drop, recurrence interval, and size distribution, and analyzed spatiotemporal changes in earthquake productivity and size distribution of an aftershock population triggered by a major earthquake (modeled as a uniform stress increase applied instantaneously to the entire computational grid). Here, motivated by the data summarized in the Observed Earthquake Interactions section, we shall present the results of similar spatiotemporal analyses of numerical composite catalogs in which each earthquake, or each earthquake above a specified size, is treated as a mainshock. Before we proceed, a summary of some of the results of Ziv and Rubin (2003) is needed.

$B/A$ . For instability to occur, the ratio  $B/A$  should be larger than 1. A large  $B/A$  implies a large tendency for instability. It is therefore easier for ruptures starting with a single element to grow larger if they are surrounded by elements with a high  $B/A$ . As a result, increasing  $B/A$  increases the range of earthquake sizes.

$A\sigma\dot{\delta}_{\text{seis}}/\dot{\tau}_{\text{tect}}D_c$ . This parameter is a ratio between two timescales. One timescale is  $t_a = A\sigma/\dot{\tau}_{\text{tect}}$ , which is the characteristic time for aftershock duration accounting for the effect of interaction among aftershocks. The other timescale,  $D_c/\dot{\delta}_{\text{seis}}$ , may be thought of as the characteristic contact time of an asperity of size  $D_c$  during seismic slip. Short contact time during seismic slip implies high healing rates when slip

stops. Thus, increasing  $t_a$  with respect to  $\delta_{\text{seis}}/D_c$  results in longer recurrence intervals and larger stress drops.

*W/L.* Fault elements are subject to a constant tectonic stressing rate and stress steps due to slip on other fault elements. The contribution to the long-term effective stressing rate from interaction with other fault elements increases in rough proportion to  $W/L$ . Thus, increasing  $W/L$  increases the seismicity rate and increases the range of rupture sizes. If  $W/L$  is too large ( $\geq 10$ ), ruptures become unstoppable.

#### Spatiotemporal Analysis of Earthquake Production and the Consequences of Treating Microearthquakes as Potential Mainshocks

The standard approach is to regard only moderate to large events as mainshocks. Thus, the approach taken here of treating each earthquake as a potential mainshock is a rather unusual one. What are the consequences of this approach? We use synthetic catalogs to address this question. We converted the synthetic catalogs into stacked catalogs, using an algorithm that is identical to the one we use for the conversion of the natural catalogs. We computed seismicity rate in the synthetic stacked catalogs for nonoverlapping consecutive time windows that increase at a logarithmic rate. Plots of seismicity rate change as a function of lag time normalized by  $t_a$  are shown in Figure 9. Seismicity rates computed for a composite catalog produced by stacking the aftershocks of events that ruptured single cells are shown in Figure 9a, whereas seismicity rates calculated for catalogs that were produced by stacking the aftershocks of earthquakes with rupture dimensions greater than or equal to 9 cells and greater than or equal to 16 cells are shown in Figure 9b,c, and respectively. These plots show that the main consequence of stacking the aftershock sequences of microearthquakes is to increase the seismicity rate in large distance bins. This difference is the result of the larger number of apparent mainshock–aftershock pairs (see Fig. 2) in catalogs that are produced by stacking the aftershock sequences of small events and due to the increased fraction of these pairs with increasing distance from small mainshocks. Thus, using our approach of stacking the aftershock sequences of microearthquakes, the interaction at large distances is exaggerated.

Another important result concerns the duration of aftershock activity. While our data analysis shows that aftershocks of microearthquakes do not last more than 100 days, it is known that aftershock sequences associated with large earthquakes may last for years. Moreover, Dieterich (1994) presented evidence for the existence of a linear scaling between aftershock duration  $t_a$  and mainshock recurrence time  $t_r$  (figure 3 and table 2 of Dieterich [1994]). To explain this scaling, Dieterich relied on the result that aftershock duration  $t_a$  is inversely proportional to the effective stressing rate and on the inference that since earthquake stress drop is independent of earthquake size, the effective stressing rate acting on an earthquake is inversely proportional to the recurrence

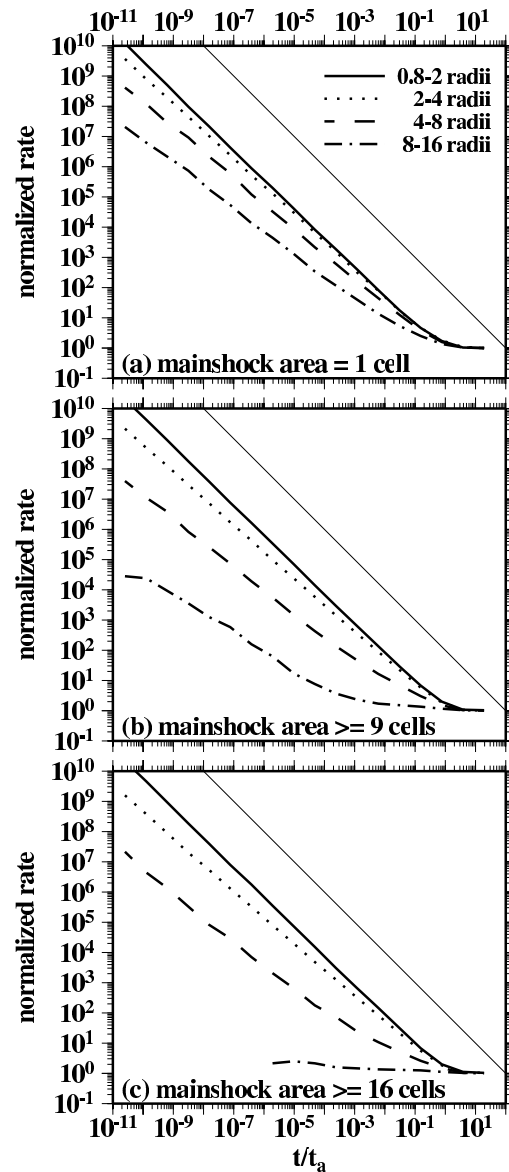


Figure 9. Simulated seismicity rates as function of normalized time, for stress overshoot between 5% and 30%,  $W/L = 10$ ,  $B/A = 10$ , and  $t_a \delta_{\text{seis}}/D_c = 10^{15}$  and for composite catalogs produced by stacking aftershock sequences of mainshocks with rupture area (a) equal to 1 cell, (b) greater than or equal to 9 cells, and (c) greater than or equal to 16 cells.

interval  $t_r$  of that earthquake. This linear relation between  $t_a$  and  $t_r$  can translate into a relation between  $t_a$  and earthquake magnitude if one assumes that the effective stressing rate on large earthquakes is smaller than that on small earthquakes, or equivalently that the recurrence interval of small earthquakes is smaller than that of large earthquakes. This assumption is certainly borne out for small to moderate repeating earthquakes in California (Ellsworth, 1994; Nadeau and Johnson, 1998), which in many cases seem to represent characteristic earthquakes being loaded by creep of a surrounding fault as well as by a remotely applied load. In the

current model, however, since earthquakes do not break characteristic fault patches, a direct relation between recurrence interval (or earthquake size) and effective loading rate does not exist. Thus, aftershock duration appears to be independent of mainshock size (Fig. 9). Such a relation might be recovered using a model where cells are of unequal sizes. Alternatively, it is possible that a scaling between mainshock size and aftershock duration may arise in a more realistic crustal-scale model with a finite fault depth and depth-dependent properties, where (as in Rice [1993]) the largest earthquake breaks the full seismogenic thickness and induces postseismic slip underneath.

As mentioned before, Dieterich's model predicts constant seismicity rate following a stress step. In practice, however, this feature may be hard or impossible to observe in areas subjected to very large  $\Delta\tau/A\sigma$ , because the seismicity rate remains constant over a time interval that is inversely proportional to  $\exp(\Delta\tau/A\sigma)$  (equation 18 of Dieterich [1994]). In order to examine the consequences of stacking the aftershocks of mainshocks of different sizes, it was necessary to produce a catalog that has a wide range of event sizes. Thus, in producing Figure 9, we set the values of both  $B/A$  and  $t_a\dot{\delta}_{\text{seis}}/D_c$  to be large. This choice of parameters gives rise to a very large  $\Delta\tau/A\sigma$  in the vicinity of the mainshock and therefore to the lack of flattening of the seismicity curves at short time lags. Seismicity curves calculated as before for numerical catalogs produced with different values of  $B/A$  and  $t_a\dot{\delta}_{\text{seis}}/D_c$  are shown in Figure 10. Flattening of the seismicity curves at the short time window may be seen in Figures 10b and 10c.

Another feature that may be seen in Figure 10 is the decrease of seismicity rate below the background level near a time lag of  $t_a$  in the nearest distance bin. The decrease below the background seismicity rate is caused by the abnormally high ratio of small to large earthquakes during this time window, which we explain in the next section. Note that a similar decrease below the background rate is observed for the San Andreas and the Calaveras faults in the distance range of 0.8–2 radii (Fig. 3).

Figure 10 shows that the effect of increasing both  $B/A$  and  $t_a\dot{\delta}_{\text{seis}}/D_c$  is to raise the seismicity rate curves. The increase in the seismicity response due to increasing  $B/A$  is related mainly to the effect of  $B/A$  on the earthquake size distribution. Because increasing  $B/A$  increases the range of earthquake sizes, in the larger distance ranges it also increases the number of pairs that we referred to as apparent aftershocks (Fig. 2). In the nearest distance range, a broader size distribution results in larger stress changes. In Figure 10c,  $B/A$  is such that all ruptures occupy only a single cell. For the stress drops of this simulation, the stress change on the nearest-neighbor cell is such that it would give rise to an instantaneous rate change of  $\sim 10^7$ , if this was the only stress change acting on the aftershock. The agreement with Figure 10c suggests that the contribution of apparent aftershocks to the rate change is insignificant in this case. As mentioned earlier, the effect of increasing  $t_a\dot{\delta}_{\text{seis}}/D_c$  is to increase the

stress drop. The increase of the seismicity rate with increasing  $t_a\dot{\delta}_{\text{seis}}/D_c$  is a direct consequence of this effect.

The variability in the seismicity response to a stress change seen in Figure 10 resembles to some degree the type of variability observed along the Calaveras, the Sargent, and the San Andreas faults (Fig. 3). Thus, although the observed variability in spatiotemporal clustering may be attributable to differences in fault structure and other heterogeneities that are not accounted for in our model, it is also possible that it reflects differences in the fault constitutive properties.

#### Spatiotemporal Analysis of Earthquake Size Distribution

The effect of a stress increase is to increase the seismicity rate, which leads to a higher effective stressing rate on nearby potential earthquake sites. The combined effect of a stress step followed by a higher effective stressing rate is to strengthen cells that are near failure and to weaken cells that are far from failure (Ziv and Rubin, 2003). Cells that fail shortly after a previous nearby earthquake are most commonly cells that were close to failure at the time of that earthquake. Because these cells have undergone strengthening, they release larger seismic moment than the pre-mainshock average and are therefore more likely to trigger adjacent cells and form large ruptures. In addition, because of the mainshock-induced stress change, the cells surrounding an aftershock nucleation site are on average closer to failure than the cells surrounding an earthquake in the background. Both of these effects give rise to an overall wider range of earthquake sizes early during an aftershock sequence. On the other hand, cells that fail long after a nearby earthquake were early in the cycle at the time of that earthquake. Because these cells have undergone weakening, they release seismic moment that is smaller than average and are therefore less likely to expand to adjacent cells. Thus, the weakening of these cells gives rise to an overall smaller range of earthquake sizes late during the aftershock sequence. For these reasons, the effect of a stress step is not only to perturb the seismicity rate, but also to modify the earthquake size distribution.

Average seismic moment in the synthetic catalogs is computed for nonoverlapping consecutive time windows that increase at a logarithmic rate. Plots of fractional changes, with respect to the catalog long-term average, in the average seismic moment as a function of lag time normalized by  $t_a$  are shown in Figure 11 for areas confined to 1–2 radii of a previous mainshock and for various values of  $B/A$  and  $t_a\dot{\delta}_{\text{seis}}/D_c$ . Average seismic moment shortly following a previous earthquake is significantly higher than the catalog average. In all cases, but most notably in the top two panels, average seismic moment later decreases below the long-term average before reaching a steady state. The higher average moment at early times is due to earthquakes occurring on cells that were strengthened by a previous nearby earthquake, whereas the lower-than-average moment at later

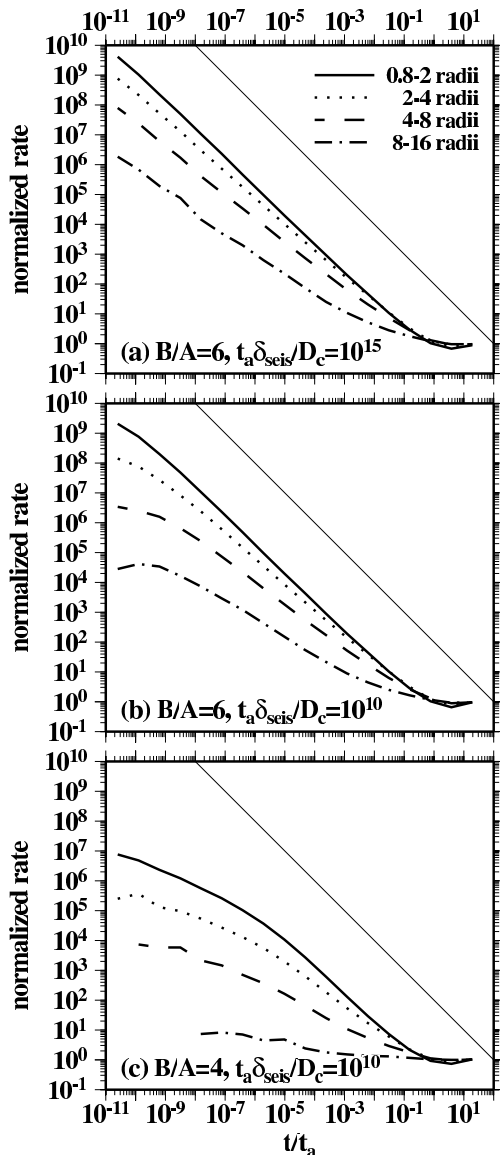


Figure 10. Simulated seismicity rates as function of normalized time, for stress overshoot between 5% and 30%,  $W/L = 10$ , and different values of  $B/A$  and  $t_a \delta_{seis}/D_c$ . The thin solid line represents a slope of  $1/\text{time}$ .

times is due to earthquakes occurring on cells that were weakened by a previous nearby earthquake.

We wish to point out an important difference between the results obtained with  $B/A = 6$  and those obtained with  $B/A = 4$ . While time-dependent changes in seismic moment for  $B/A = 6$  are due to both changes in fault strength and rupture dimensions, those for  $B/A = 4$  are due entirely to changes in fault strength. This is because the effect of decreasing  $B/A$  is to reduce the tendency of ruptures to expand, such that for  $B/A \leq 4$  all ruptures consist of single elements. This explains why the magnitude of the variations in seismic moment for  $B/A = 4$  is smaller than that for  $B/A = 6$  and also why the average moment for  $B/A = 4$  first increases

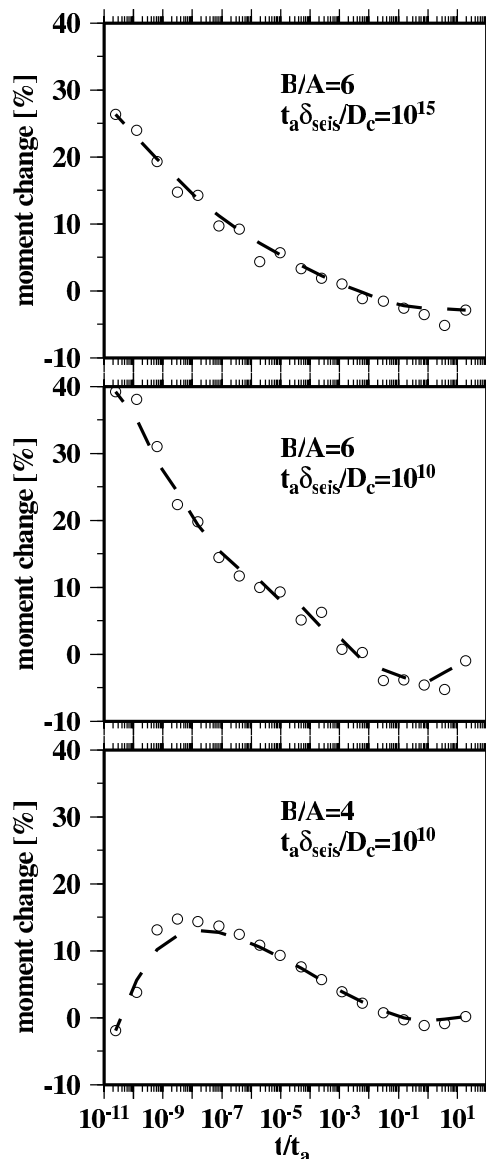


Figure 11. Fractional changes in average moment, with respect to the catalog average, as a function of normalized time, confined to 1–2 radii of a previous earthquake. Stress overshoot ranges between 5% and 30%,  $W/L = 10$ , and values of  $B/A$  and  $t_a \delta_{seis}/D_c$  are the same as in Figure 10. The dashed lines are highly smoothed fits to the data.

and then decreases (this issue is discussed in greater depth in Ziv and Rubín [2003]).

An example of simulated frequency-size distributions of events occurring in areas confined to 0.8–3 radii from a previous event are shown in Figure 12 for two consecutive time windows. Note that the ratio of large to small earthquakes early during the aftershock sequence is larger than that later during the sequence. These results are consistent with our observations, as well as with reports by Wiemer and Katsumata (1999) of lower  $b$ -values immediately following a stress increase.

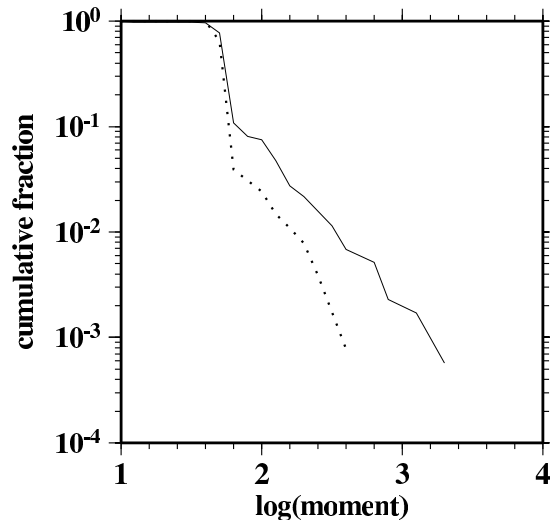


Figure 12. Plots of frequency-size distributions of simulated earthquakes in areas confined to 1–3 radii from a previous earthquake for time intervals of 0– $0.1t_a$  (solid) and  $0.1t_a$ – $1t_a$  (dotted). In this example stress overshoot ranges between 5% and 30%,  $W/L = 10$ ,  $B/A = 6$ , and  $t_a \dot{\sigma}_{seis}/D_c = 10^{10}$ .

### Summary and Conclusions

We describe a method of analyzing the spatiotemporal productivity and size distribution of aftershocks in catalogs of relocated microseismicity. According to this scheme, each earthquake is treated as if it were a mainshock. Lag times between mainshock–aftershock pairs are stacked to give a composite catalog. The main disadvantage of this method is that it exaggerates the degree of earthquake interaction at great distances. The main advantage is that it greatly enhances the statistics due to the fact that the size of the composite catalog is much larger than the size of the original catalog.

We compare the stress dependence of seismicity rate change along sections of the Sargent fault, the Calaveras fault, and the San Andreas fault. In all three cases, the seismicity rate decays asymptotically as  $1/\text{time}$ , and the duration of the aftershock activity appears to be independent of distance from the mainshock. In addition, seismicity rate curves flatten at lag times smaller than 100 sec. We note that these observations are predicted by Dieterich's (1994) model of aftershock production. In addition we find that for the San Andreas and the Calaveras catalogs, the return of seismicity to the background level in the nearest distance range appears to be preceded by a period during which the seismicity rate falls about 30% below the background rate.

We examine the effect of a stress step on earthquake size distribution along these faults. We find that the  $b$ -value during the  $10^3$ - to  $10^4$ -sec interval following a previous earthquake is significantly lower than that of the long term.

We present an inherently discrete quasi-static fault model, in which the fault surface is governed by rate- and

state-dependent friction. Similar to what is observed, we find that periods of elevated seismic activity in an aftershock sequence may be followed by periods during which the seismicity rate is lower than the long-term average rate and that the  $b$ -values early in the aftershock sequence are smaller than the  $b$ -values later in the sequence. The changes in the  $b$ -values are due to the combined effect of a stress change followed by a higher effective stressing rate (due to higher seismicity rates) on the fault strength. We conclude that the observed response to a stress step is consistent with the notion of crustal faults being governed by rate- and state-dependent friction.

### Acknowledgments

This study benefited from discussions with Jim Dieterich. Comments from Andrew J. Michael, Greg Anderson, and an anonymous reviewer helped to improve the manuscript.

### References

- Abercrombie, R. E. (1996). The magnitude-frequency distribution of earthquakes recorded with deep seismometers at Cajon Pass, southern California, *Tectonophysics* **261**, 1–7.
- Carena, S., and J. Suppe (2002). 3D imaging of active structures using earthquake aftershocks: the Northridge thrust, California, *J. Struct. Geol.* **24**, no. 4, 887–904.
- Cochard, A., and R. Madariaga (1996). Complexity of seismicity due to highly rate dependent friction, *J. Geophys. Res.* **101**, 25,321–25,336.
- Dieterich, J. H. (1979). Modeling of rock friction. I. Experimental results and constitutive equations, *J. Geophys. Res.* **84**, 2161–2168.
- Dieterich, J. H. (1992). Earthquake nucleation on faults with rate- and state-dependent strength, *Tectonophysics* **211**, 115–134.
- Dieterich, J. H. (1994). A constitutive law for rate of earthquake production and its application to earthquake clustering, *J. Geophys. Res.* **99**, 2601–2618.
- Dieterich, J. H. (1995). Earthquake simulations with time-dependent nucleation and long-range interaction, *Nonlinear Proc. Geophys.* **2**, 109–120.
- Ellsworth, W. L. (1994). Characteristic earthquakes and long-term earthquake forecasts: implications of central California seismicity, in *Urban Disaster Mitigation*, F. Y. Cheng and M.-S. Sheu (Editors), Elsevier, Amsterdam, 1–14.
- Eshelby, J. (1957). The determination of elastic field of an ellipsoidal inclusion and related problems, *Proc. R. Soc. London A* **241**, 379–396.
- Gomberg, J., M. L. Blanpied, and N. M. Beeler (1997). Transient triggering of near and distant earthquakes, *Bull. Seism. Soc. Am.* **87**, 294–309.
- Got, J.-L., J. Fréchet, and F. Klein (1994). Deep fault geometry inferred from multiplet relative relocation beneath the south flank of Kilauea, *J. Geophys. Res.* **99**, 15,375–15,386.
- Gross, S., and C. Kisslinger (1997). Estimating tectonic stress rate and state with Landers aftershocks, *J. Geophys. Res.* **102**, 7603–7612.
- Hosono, K., and Yoshida, A. (2002). Do large aftershocks decrease similarly to smaller ones? *Geophys. Res. Lett.* **29**, no. 10, doi 10.1029/2001GL014403.
- Jennings, C. W. (1992). Preliminary fault activity map of California, Open-File Rept. 92–93, California Department of Conservation, Division of Mines and Geology, Sacramento.
- Kilb, D., and A. M. Rubin (2002). Implications of diverse fault orientations imaged in relocated aftershocks of the Mt. Lewis,  $M_L$  5.7, California, earthquake, *J. Geophys. Res.* **107**, no. B11, doi 10.1029/2001JB000149.
- Madariaga, R. (1976). Dynamics of an expanding circular fault, *Bull. Seism. Soc. Am.* **66**, 639–666.

- Nadeau, R. M., and L. R. Johnson (1998). Stress studies at Parkfield. VI. Moment release rates and estimates of source parameters for small repeating earthquakes, *Bull. Seism. Soc. Am.* **88**, 790–814.
- Rice, J. R., and S. T. Tse (1986). Dynamic motion of a single degree of freedom system following a rate and state dependent friction law, *J. Geophys. Res.* **91**, 521–530.
- Rubin, A. M., D. Gillard, and J.-L. Got (1999). Streaks of microearthquakes along creeping faults, *Nature* **400**, 635–641.
- Rubin, A. M. (2002). Aftershocks of microearthquakes as probes of the mechanics of rupture, *J. Geophys. Lett.* **107**, no. B7, doi 10.1029/2001JB000496.
- Ruina, A. L. (1980). Friction laws and instabilities: a quasistatic analysis of some dry frictional behavior, *Ph.D. Thesis*, Brown University, Providence, Rhode Island.
- Ruina, A. (1983). Slip instability and state variable friction laws, *J. Geophys. Res.* **88**, 10,359–10,370.
- Schaff, D. P., G. C. Beroza, and B. E. Shaw (1998). Postseismic response of repeating aftershocks, *Geophys. Res. Lett.* **25**, 4549–4552.
- Seeber, L., and J. G. Armbruster (1995). The San Andreas fault system through the Transverse Ranges as illuminated by earthquakes, *J. Geophys. Res.* **100**, 8285–8310.
- Shaw, J. H., and P. M. Shearer (1999). An elusive blind-thrust fault beneath metropolitan Los Angeles, *Science* **283**, 1516–1518.
- Shearer, P. M. (1998). Evidence from a cluster of small earthquakes for a fault at 18 km depth beneath Oak Ridge, southern California, *Bull. Seism. Soc. Am.* **88**, 1327–1336.
- Toda, S., R. S. Stein, P. A. Reasenberg, J. H. Dieterich, and A. Yoshida (1998). Stress transferred by the 1995  $M_w = 6.9$  Kobe, Japan, shock: effect on aftershocks and future earthquake probabilities, *J. Geophys. Res.* **103**, 24,543–24,565.
- Waldhauser, F., W. L. Ellsworth, and A. Cole (1999). Slip-parallel seismic lineations on the northern Hayward fault, California, *Geophys. Res. Lett.* **26**, 3525–3528.
- Wiemer, S., and K. Katsumata (1999). Spatial variability of seismicity parameters in aftershock zones, *J. Geophys. Res.* **104**, 13,135–13,152.
- Ziv, A., and A. M. Rubin (2003). Implications of rate-and-state friction for properties of aftershock sequence: quasi-static inherently discrete simulations, *J. Geophys. Res.* **108**, 2051, doi 10.1029/2001JB001219.

Department of Geosciences  
Guyot Hall  
Princeton University  
Princeton, New Jersey 08544

Manuscript received 13 May 2002.